

End-to-End Deep Learning for Interior Tomography with Low-Dose X-ray CT

Yoseob Han, Dufan Wu, Kyungsang Kim, and Quanzheng Li

Department of Radiology, Center for Advanced Medical Computing and Analysis (CAMCA), Harvard Medical School and Massachusetts General Hospital, Boston, MA, USA

E-mail: {yhan5, dwu6, kkim24, li.quanzheng}@mgh.harvard.edu

September 2021

Abstract. Objective: There exist several X-ray computed tomography (CT) scanning strategies to reduce a radiation dose, such as (1) sparse-view CT, (2) low-dose CT, and (3) region-of-interest (ROI) CT (called interior tomography). To further reduce the dose, the sparse-view and/or low-dose CT settings can be applied together with interior tomography. Interior tomography has various advantages in terms of reducing the number of detectors and decreasing the X-ray radiation dose. However, a large patient or small field-of-view (FOV) detector can cause truncated projections, and then the reconstructed images suffer from severe cupping artifacts. In addition, although the low-dose CT can reduce the radiation exposure dose, analytic reconstruction algorithms produce image noise. Recently, many researchers have utilized image-domain deep learning (DL) approaches to remove each artifact and demonstrated impressive performances, and the theory of deep convolutional framelets supports the reason for the performance improvement.

Approach: In this paper, we found that the image-domain convolutional neural network (CNN) is difficult to solve coupled artifacts, based on deep convolutional framelets.

Significance: To address the coupled problem, we decouple it into two sub-problems: (i) **image domain noise reduction *inside truncated projection* to solve low-dose CT problem** and (ii) **extrapolation of projection *outside truncated projection* to solve the ROI CT problem**. The decoupled sub-problems are solved directly with a novel proposed end-to-end learning using dual-domain CNNs.

Main results: We demonstrate that the proposed method outperforms the conventional image-domain deep learning methods, and a projection-domain CNN shows better performance than the image-domain CNNs which are commonly used by many researchers.

1. Introduction

X-ray CT imaging provides high-quality and high-resolution images, but X-ray CT causes potential cancer risks due to radiation exposures [1]. Thus, many researchers have studied to reduce the radiation dose [2], where three approaches were widely used by reducing (1) projection views (sparse-view CT), (2) photon counts of X-ray source (low-dose CT), and (3) ROI (interior tomography). Unlike the low-dose CT reducing photon counts and the sparse-view CT undersampling projection views, the interior tomography retains these factors but uses small FOV detectors, which are useful for imaging of small target regions such as cardiac and dental imagings. In addition, portable C-arm CTs also use interior tomography imaging to miniaturize the hardware system. Therefore, interior tomography not only reduces the radiation exposures but also has a cost-benefit due to the small size of detectors. In addition, the sparse-view and/or low-dose settings can be applied together to interior tomography, and then the radiation exposure dose is extremely reduced compared to using interior tomography only. While interior tomography has various advantages, truncated projection data has not been correctly reconstructed using analytic CT reconstruction algorithms such as filtered backprojection (FBP) and the reconstructed image suffers from severe cupping artifacts. In addition, the reconstructed images from multiple incomplete CT measurements show additional artifacts such as streaking artifacts due to sparse-view and/or image noise caused by low-dose.

A simple method to mitigate the cupping artifacts caused by interior tomography is projection extrapolation [3]. Even though the reconstructed image using extrapolated projection data shows moderated cupping artifacts, Hounsfield units (HU) can be biased due to inaccurate extrapolation [4]. Other researchers have developed model-based iterative reconstruction (MBIR) methods with several penalty terms such as total variation (TV) [5] and generalized L-spline [6, 7]. Similar to interior tomography, various MBIR methods have been investigated to address streaking [8, 9, 10, 11, 12] and image noise [13, 14]. However, a drawback of MBIR-based methods is that it requires a long reconstruction time due to the computationally intensive CT operators like projector and backprojector.

Recently, DL algorithms have been proposed as high-performance solutions for sparse-view CT [15, 16, 17], low-dose CT [18, 19, 20], and interior tomography [21, 22]. The solutions based on DL have surpassed the conventional MBIR methods [5, 6, 7, 8, 9, 10, 11, 12, 13, 14] in terms of image quality and reconstruction time. Although the DL methods have been applied to the image domain to remove each artifact and achieve excellent performance, a fundamental reason for the artifacts is incomplete measurements of a projection domain like a small number of views, photons, and small-sized detectors. In addition, if the projection y is distorted by two or more collapsed factors as shown in Fig. 1(a), the FBP image q_j in Fig. 1(b) is contaminated by mixed artifacts by a cupping artifact c_j and an image noise n_j . More specifically, the cupping artifact c_j is described as a single global artifact but the image noise n_j

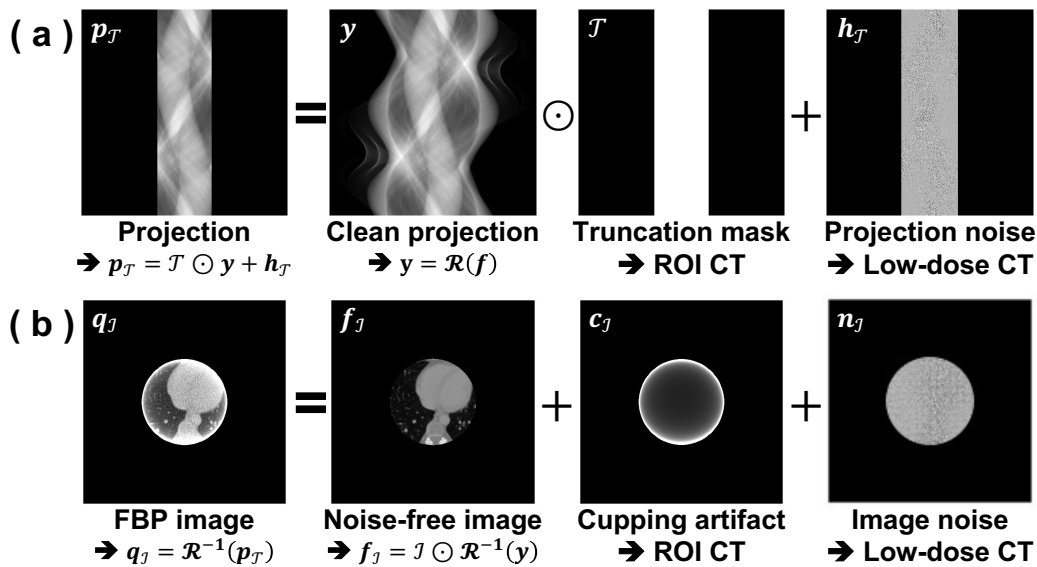


Figure 1. Low-dose ROI CT compositions of (a) measurement $p_{\mathcal{T}} = \mathcal{T} \odot y + h_{\mathcal{T}}$ in projection domain and (b) FBP image $q_{\mathcal{J}} = f_{\mathcal{J}} + c_{\mathcal{J}} + n_{\mathcal{J}}$ in image domain.

appears as dispersion artifacts. In other words, the blended artifact ($c_{\mathcal{J}} + n_{\mathcal{J}}$) has all of the opposite properties. Theoretically, the deep convolutional framelets [23], which is a mathematical framework for understanding deep learning behavior, has proved that the low-rankness is a crucial factor for high performance, however, the combined opposite features are difficult to satisfy the low-rankness. Therefore, it is difficult for a single model to learn an optimal feature that contains features composed of opposite distributions.

In this paper, we propose a novel end-to-end deep learning method to solve a coupled low-dose ROI CT problem, simultaneously. Since a standard CNN architecture like Fig. 2(a) is difficult to solve the coupled CT problem in an image domain due to unsatisfying a low rankness based on deep convolutional framelets [23], a novel projection-domain CNN (see Fig. 2(b)) is proposed to eliminate a mixture of artifacts combining the cupping artifact and the image noise by estimating two decoupled projection domain solutions: (i) **image domain noise reduction *inside* a measured region \mathcal{T}** and (ii) **extrapolation of projection *outside* the measured region $(1 - \mathcal{T})$** . After the projection-domain CNN, an image-domain CNN is applied to an image reconstructed by the projection-domain CNN. Therefore, the proposed network consists of a projection-domain CNN and an image-domain CNN, and its flowchart is illustrated in Fig. 2(d). To compare the same architecture with the proposed network, Fig. 2(c) (called W-Net) is used as the comparison architecture.

This paper is structured as follows. In Section 2, interior tomography and low-dose X-ray CT problems are defined, and the theory of deep convolutional framelets are briefly reviewed. Section 4 describes the limitations of conventional image-domain CNNs and how the proposed method addresses the problem when solving the low-dose

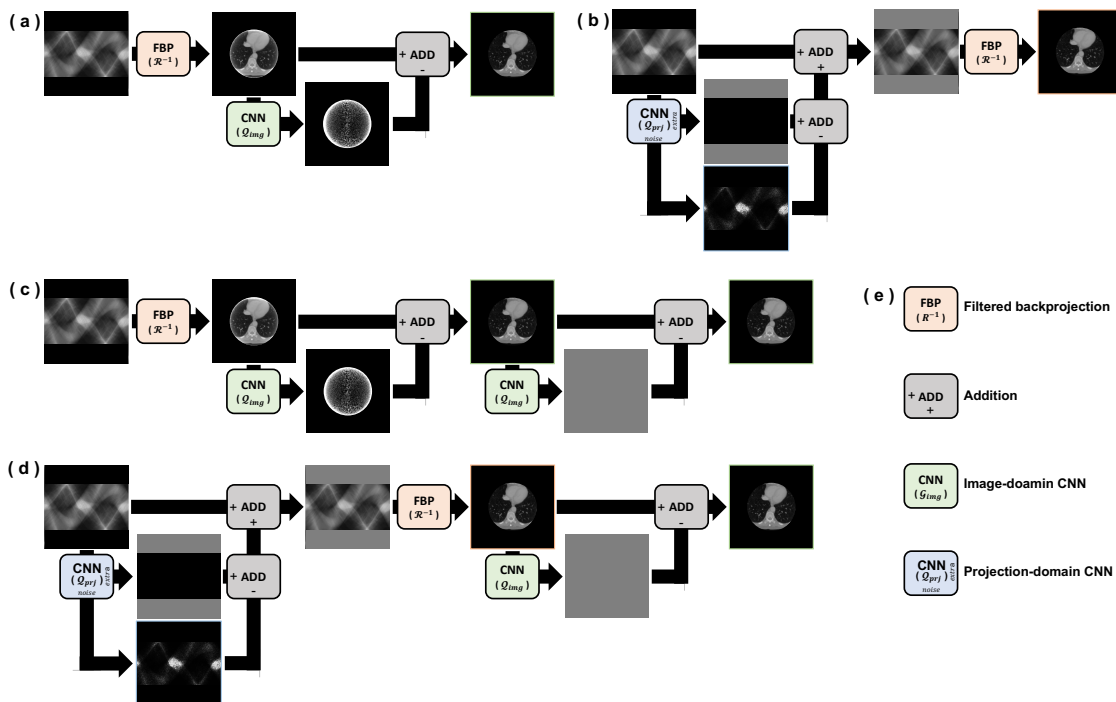


Figure 2. Various neural network architectures. (a) image-domain CNN, (b) projection-domain CNN, (c) W-Net, and (d) proposed network (called Dual-Net). (e) describes function modules used in (a-d).

ROI CT problem. Then, Section 3 describes the methods to implement and validate the proposed method, and experimental results are followed in Section 5. Discussions and conclusions are provided in Sections 6 and 7.

2. Theory

2.1. Interior tomography

Here, we first describe Radon transform \mathcal{R} and then extend it to the interior tomography problem using a truncated Radon transform $\mathcal{T}_\mu \mathcal{R}$. Let θ denotes a vector on the unit sphere $\mathbb{S} \in \mathbb{R}^2$. The set of orthogonal vectors θ^\perp is described as

$$\theta^\perp = \{\mathbf{v} \in \mathbb{R}^2 : \mathbf{v} \cdot \theta = 0\}, \quad (1)$$

where \cdot denotes an inner product. If an image is defined by $f(\mathbf{x})$ for $\mathbf{x} \in \mathbb{R}^2$, the Radon transform \mathcal{R} of the image f is formulated as

$$\mathcal{R}f(\theta, u) := \int_{\theta^\perp} d\mathbf{v} f(\mathbf{v} + u\theta), \quad (2)$$

where $u \in \mathbb{R}$ and $\theta \in \mathbb{S}$. The Radon transform \mathcal{R} can be reformulated as a X-ray transform D_f , is defined as

$$D_f(\theta, \mathbf{a}) = \int_0^\infty dt f(\mathbf{a} + t\theta), \quad (3)$$

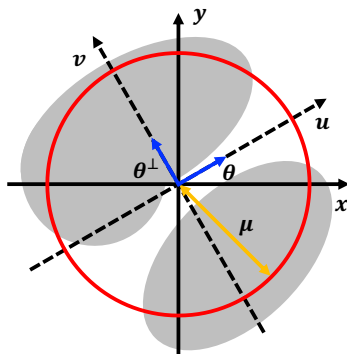


Figure 3. A CT coordinate system.

where $\mathbf{a} \in \mathbb{R}^2$ denotes a X-ray source position.

If the Radon transform $\mathcal{R}f$ is restricted by $\{(\theta, u) : |u| < \mu\}$ as shown in Fig. 3, then a truncated Radon transform is defined as $\mathcal{T}_\mu \mathcal{R}f$, where \mathcal{T}_μ is truncation mask with radius μ . Therefore, an interior tomography problem can be explained to find an unknown image $f(\mathbf{x})$ for $|\mathbf{x}| < \mu$ from the truncated Radon transform $\mathcal{T}_\mu \mathcal{R}f$. However, the truncated Radon transform $\mathcal{T}_\mu \mathcal{R}f$ causes a null space \mathcal{N} , and the null space \mathcal{N} makes the interior tomography problem a strong ill-posed problem. The null space image \mathcal{N} can be illustrated like a cupping artifact c_j as shown in the Fig 1(b). Cupping artifacts appear as single global artifacts on CT images and are particularly the singularities at ROI boundaries. In particular, the artifacts are mainly related to how much of the patients are truncated and the density of the truncated tissue.

2.2. Low-dose X-ray CT

When a X-ray source satisfies monochromatic condition and there is no projection noise, i.e. the number of incident photons I_0 is sufficiently large, the number of transmitted photons I measured by detectors follows Poisson distribution [24], is described as

$$I \sim \text{Poisson}(I_0 * \exp^{-[D_f]}). \quad (4)$$

If the measurement I is not distorted by projection noise, Eq. 4 is linearized by a negative logarithmic transform as

$$y = -\ln\left(\frac{I}{I_0}\right) = -\ln(\exp^{-[D_f]}) = D_f = \mathcal{R}f. \quad (5)$$

Since a projection data y satisfies Radon transform \mathcal{R} of the image f , the image f can be reconstructed analytically by applying an inverse Radon transform \mathcal{R}^{-1} .

If the number of incident photons I_0 is not enough to collect the noise-free projection data y , i.e. low-dose X-ray CT, the projection data y is collapsed by non-stationary Gaussian noise h like [20, 25]:

$$p \approx y + h. \quad (6)$$

Since the collapsed projection p no longer satisfies Radon transform \mathcal{R} relationship of the image f , its reconstructed image q from the collapsed projection p is consisted of

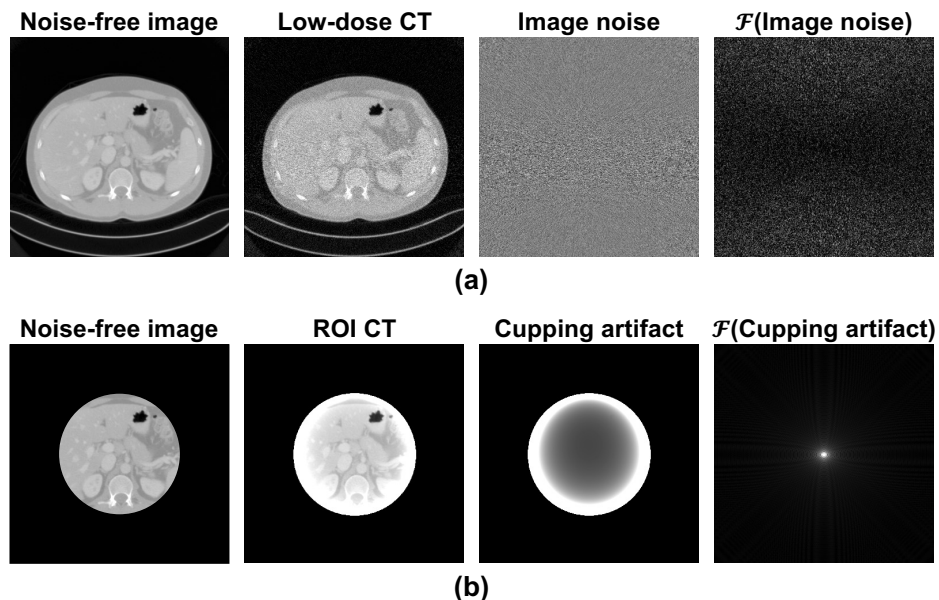


Figure 4. (a) Image noise property of low-dose CT and (b) Cupping artifact property of ROI CT. \mathcal{F} denotes 2D Fourier transform.

clean image f and image noise n :

$$q = \mathcal{R}^{-1}(p) \approx \mathcal{R}^{-1}(y + h) = f + n. \quad (7)$$

As shown in Fig. 1(b), the image noise n_j appear as dispersion artifacts in all areas of the CT images, in contrast to cupping artifacts c_j , which are a single global artifacts in interior tomography.

2.3. Deep convolutional framelets

Deep convolutional framelets [23, 26] provided a mathematical link between classical signal processing and deep learning. The mathematical link is started from the Hankel matrix approaches [27, 28, 29, 30, 31], and we start from the regression problem with low-rank Hankel structured matrix constraint defined below:

$$\begin{aligned} \arg \min_{\bar{f} \in \mathbb{R}^n} \quad & \|f - \bar{f}\|^2 \\ \text{subject to} \quad & \text{RANK}\mathbb{H}_d(\bar{f}) = r < d, \end{aligned} \quad (8)$$

where $f \in \mathbb{R}^n$ and $\bar{f} \in \mathbb{R}^n$ are a noise-free image and a denoised solution, respectively, r denotes the rank of the Hankel structured matrix $\mathbb{H}_d(\bar{f}) \in \mathbb{R}^{n \times d}$, and d is a matrix pencil parameter. Specifically, the rank of the Hankel structured matrix $\text{RANK}\mathbb{H}_d(\bar{f})$ is determined by the number of non-zero components in Fourier domain of the solution $\mathcal{F}(\bar{f})$:

$$\text{RANK}\mathbb{H}_d(\bar{f}) = \text{COUNT}(\mathcal{F}(\bar{f}) \neq 0). \quad (9)$$

If there is any feasible solution \bar{f} , the singular value decomposition (SVD) of its Hankel structured matrix $\mathbb{H}_d(\bar{f})$ is calculated by $\text{SVD}(\mathbb{H}_d(\bar{f})) = U\Sigma V^T$, where $U \in \mathbb{R}^{n \times r}$

and $V \in \mathbb{R}^{d \times r}$ are the left and right singular vector bases matrices, respectively, and $\Sigma = (\sigma) \in \mathbb{R}^{r \times r}$ denotes the diagonal matrix of singular values. Here, we consider two matrices pairs $\Phi, \tilde{\Phi} \in \mathbb{R}^{n \times n}$ and $\Psi, \tilde{\Psi} \in \mathbb{R}^{d \times r}$ satisfying conditions below:

$$(a) \tilde{\Phi}\Phi^T = I_{n \times n}, \quad (b) \Psi\tilde{\Psi}^T = P_{R(V)}, \quad (10)$$

where $R(V)$ denotes the range space of V and $P_{R(V)}$ is a projection onto $R(V)$. Using Eq. 10, we can formulate an equality of the Hankel structured matrix $\mathbb{H}_d(\bar{f})$, is defined as:

$$\mathbb{H}_d(\bar{f}) = \tilde{\Phi}\Phi^T\mathbb{H}_d(\bar{f})\Psi\tilde{\Psi}^T. \quad (11)$$

Specifically, Φ and $\tilde{\Phi}$ are called *non-local bases* because they multiply by the left of $\mathbb{H}_d(\bar{f})$, then interacts with all \bar{f} . In common deep learning terminology, the matrices $(\Phi, \tilde{\Phi})$ correspond to user-defined general pooling Φ and unpooling $\tilde{\Phi}$. However, Ψ and $\tilde{\Psi}$ are defined as *local bases* since they interacts with d -neighborhood of the image \bar{f} . They are referred to as learnable kernels of the convolutional layers that can be trained to satisfy Eq. 10(b). Based on Eq. 11, we can set a space \mathcal{F}_r collecting feasible images \bar{f} , is described as

$$\mathcal{F}_r = \left\{ \bar{f} \in \mathbb{R}^n \mid \bar{f} = \left(\tilde{\Phi}C \right) \otimes \nu(\tilde{\Psi}), C = \Phi^T(\bar{f} \otimes \bar{\Psi}) \right\}, \quad (12)$$

where $\bar{\Psi}$ and $\nu(\tilde{\Psi})$ denote encoder- and decoder-layer convolutional filters, respectively. The previous regression problem in Eq. 8 can be reformulated using the space \mathcal{F}_r given by

$$\arg \min_{\bar{f} \in \mathcal{F}_r} \|f - \bar{f}\|^2, \quad (13)$$

which can be represented by optimizing kernels $(\Psi, \tilde{\Psi})$ of neural network \mathcal{Q} as follows

$$\arg \min_{(\Psi, \tilde{\Psi})} \|f - \mathcal{Q}(q; \Psi, \tilde{\Psi})\|^2. \quad (14)$$

The neural network \mathcal{Q} can be trained with big datasets $\{(q^{(i)}, f^{(i)})\}_{i=1}^N$ to learn the kernels $(\Psi, \tilde{\Psi})$ representing $\text{RANK}\mathbb{H}_d(\bar{f}^{(i)}) \leq r_{\max}$, where r_{\max} is the largest rank of the Hankel structured matrix $\mathbb{H}_d(\bar{f}^{(i)})$ among the datasets and d is redefined by the convolutional filter length, is described by

$$\arg \min_{(\Psi, \tilde{\Psi})} \sum_{i=1}^N \|f^{(i)} - \mathcal{Q}(q^{(i)}; \Psi, \tilde{\Psi})\|^2. \quad (15)$$

Generally, various network architectures have been developed based on mathematical expressions or image priors, but they can be well trained with a given datasets due to their expressive power based on convolutional frames [23, 26]. In this paper, the standard U-Net [32] was used as backbone architecture in order to minimize the effects of different network architectures.

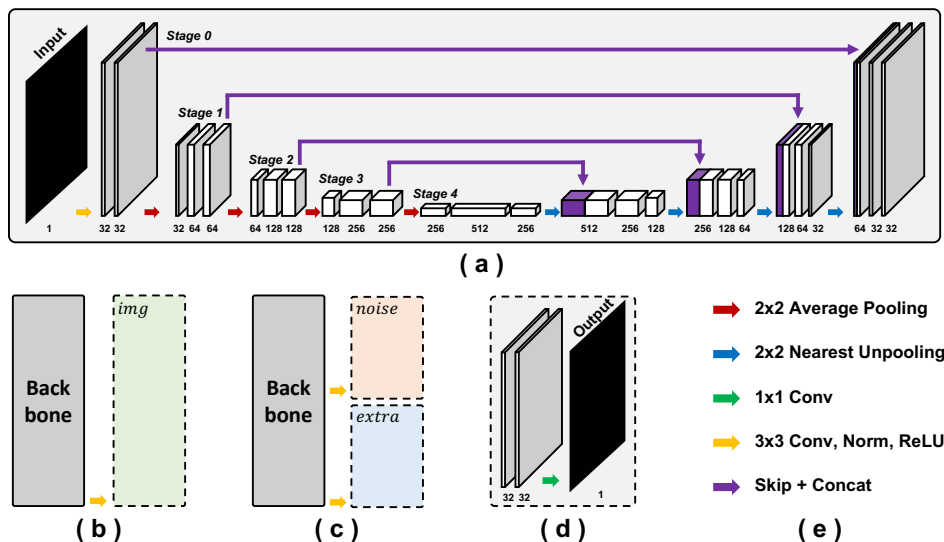


Figure 5. (a) A backbone based on the standard U-Net structure, (b) image-domain CNN Q_{img} consisting a backbone and a single bridge module to estimate an image, (c) projection-domain CNN Q_{prj} consisting the backbone and two bridge modules to estimate a projection noise inside the measured region \mathcal{T} and an extrapolation map outside the measured region $(1 - \mathcal{T})$, respectively, and (d) a bridge module. (e) shows definition of layers.

3. Materials and Methods

3.1. Datasets

Ten subject datasets from the American Association of Physicists in Medicine (AAPM) Low-Dose CT Grand Challenge [33] were used. Among ten subjects, nine subjects were used as training (8 subjects with 3,990 slices) and validation (1 subject with 252 slices) datasets. Another subject with 486 slices was used to test dataset. From the datasets, projection data were numerically generated using a forward projection operator with fan beam with equispaced geometry. A size of images is 512×512 and its pixel resolution is $1mm^2$. The number of views is 720 views and a range of rotation for X-ray source is $[0^\circ, 360^\circ)$. The number of detectors is 1440 and the detector pitch is $1mm$. The number of incident photons (I_0) is randomly defined as $10^{R(5,8)}$, where $R(a, b)$ is a uniform random number generator between a and b , and a low-dose simulation was performed according to the method of Yu *et al* [34]. Truncation ratios were used as $[0\%, R(0, 58)\%, 58\%, R(58, 74)\%, 74\%, R(74, 83)\%, 83\%]$, so datasets were extended seven times. Therefore, 27,930 ($= 3,990 \times 7$) slices and 1,764 ($= 252 \times 7$) slices are used for train and validation datasets, respectively.

For quantitative evaluation, three metrics such as the normalized mean square error (NMSE), the peak signal to noise ratio (PSNR), and the structural similarity index measure (SSIM) are used. NMSE is computed by

$$\text{NMSE}(f^*, \bar{f}) = \frac{\|f^* - \bar{f}\|_2^2}{\|f^*\|_2^2}, \quad (16)$$

where f^* and \bar{f} denote the ground truth and the estimated image, respectively. PSNR is defined as

$$\text{PSNR}(f^*, \bar{f}) = 20 \cdot \log_{10} \left(\frac{NM \|f^*\|_{\infty}}{\|f^* - \bar{f}\|_2} \right), \quad (17)$$

where N and M are the number of pixels for row and column. SSIM is formulated as

$$\text{SSIM}(f^*, \bar{f}) = \frac{(2\mu_{f^*}\mu_{\bar{f}} + c_1)(2\sigma_{f^*\bar{f}} + c_2)}{(\mu_{f^*}^2 + \mu_{\bar{f}}^2 + c_1)(\sigma_{f^*}^2 + \sigma_{\bar{f}}^2 + c_2)}, \quad (18)$$

where μ_f and σ_f^2 are a mean and a variance for $f \in [f^*, \bar{f}]$, respectively, and $\sigma_{f^*\bar{f}}$ is a covariance of f^* and \bar{f} . There are two variables to stabilize the division such as $c_1 = (k_1L)^2$ and $c_2 = (k_2L)^2$. L is a dynamic range of the pixel intensities. $k_1 = 0.01$ and $k_2 = 0.03$ are constants.

3.2. Architectures

Figs. 2(a-d) illustrate an image-domain CNN (called U-Net), a projection-domain CNN, a W-Net consisting of two image-domain CNNs, and a proposed network consisting of projection-domain CNN and image-domain CNN, respectively. Details of the image-domain CNN \mathcal{Q}_{img} and the projection-domain CNN \mathcal{Q}_{prj} illustrated in Fig. 2 are described in Figs. 5(b, c), respectively. In the proposed network in Fig. 2(d), a filtered backprojection (FBP) operation is used to transform from an output of projection-domain CNN into an input of image-domain CNN. A backbone architecture was used to standard U-Net structure [32] as shown in Fig. 5(a). The CNNs are connected to additional bridge modules (see Fig. 5(d)) after the backbone architecture. Specifically, an image-domain CNN in Fig. 5(b) has a single bridge module for estimating the image. However, a projection-domain CNN in Fig. 5(c) is attached to two bridge modules to estimate the projection noise inside measured area and the extrapolation map outside measured area, respectively. A basic layer module is consisted of 3×3 convolutional layer, batch normalization, and rectified linear unit (ReLU) as illustrated in yellow arrow of Fig. 5(e). The basic layer module is between all blocks, but the yellow arrow has been omitted for visibility. The W-Net and the proposed network use two networks as shown in Fig. 2(c-d), whereas the U-Net in Fig. 2(a) uses a single network, so the U-Net is set up to twice the size of the channels of other networks. The number of parameters of U-Net is 22,050,369, the W-Net is 11,028,034 ($= 5,514,017 + 5,514,017$) parameters, and the proposed network is 11,046,563 ($= 5,532,546 + 5,514,017$) parameters. Therefore, the number of parameters of U-Net used the doubled parameters than others.

3.3. Training

The networks were implemented using Pytorch. The proposed architecture was directly trained with an end-to-end learning scheme, so the FBP module was implemented as a custom layer type in Pytorch. In addition, a backward propagation of the FBP module can be sequentially conducted by the forward projection operator and the filtration.

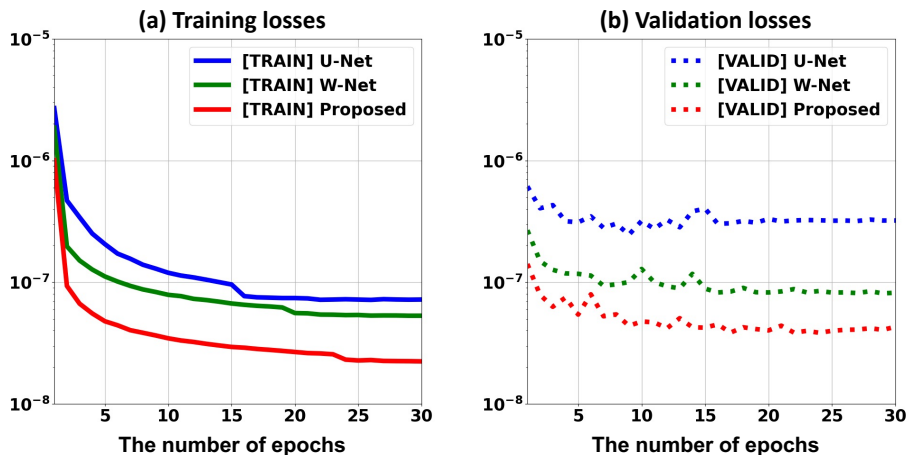


Figure 6. (a) Training losses and (b) Validation losses with respect to U-Net (blue), W-Net (green), and proposed network (red).

For two-times unrolled networks such as W-Net and proposed network, we blocked the gradient of second network from propagating to the first network during training phase in order to isolate the physical workspace of each network. A unit of a graphic processing unit (GPU) as NVIDIA Tesla V100 is used to train the network. Hyper parameters to train CNNs are described below. Adam optimizer was used. An initial learning rate was 10^{-4} and it was multiplied by 0.1 if validation loss did not decrease over 5 epochs. The number of batch sizes is 4, and the number of epochs is 30. For data augmentation, vertical flipping was applied. The above hyper parameters were applied equally to all networks as shown in Fig. 2(a,c,d) when trained.

4. Main contributions

4.1. Image-domain CNN for coupled artifact and its Limitation

The FBP image $q^{(i)}$ can be distorted by artifacts related to CT systems given by

$$q^{(i)} = f^{(i)} + g^{(i)}. \quad (19)$$

where $g^{(i)} \in [c_j^{(i)}, n^{(i)}]$ denotes artifacts according to incomplete CT systems like interior tomography and low-dose CT, $*_j$ is any images applied to ROI mask \mathcal{J} , and $c_j^{(i)}$ and $n^{(i)}$ are cupping artifacts and image noise, respectively. More specifically, the cupping artifact $c_j^{(i)}$ is described as a single global artifact on CT images and the image noise $n^{(i)}$ appears as dispersion artifacts in all area of the CT images. The artifacts have been individually conquered by various deep learning methods [18, 19, 20, 21, 22], and most of them follow a residual learning, instead of Eq. 15, given by

$$\arg \min_{(\Psi, \tilde{\Psi})} \sum_{i=1}^N \|g^{(i)} - \mathcal{Q}(q^{(i)}; \Psi, \tilde{\Psi})\|^2. \quad (20)$$

The residual learning can be interpreted to optimize the kernel $\bar{\Psi}$ which almost annihilate the noise-free image $f^{(i)}$ like

$$f^{(i)} \circledast \bar{\Psi} \simeq 0, \tag{21}$$

which is applied to Eq. 12, then the artifacts $g^{(i)}$ can be reconstructed based on the theory of deep convolutional framelets, is represented by

$$\begin{aligned} & \left(\tilde{\Phi} \left[\Phi^T \left([f^{(i)} + g^{(i)}] \circledast \bar{\Psi} \right) \right] \right) \circledast \nu(\tilde{\Psi}) \\ & \simeq \left(\tilde{\Phi} \left[\Phi^T \left(g^{(i)} \circledast \bar{\Psi} \right) \right] \right) \circledast \nu(\tilde{\Psi}) \\ & = g^{(i)}. \end{aligned} \tag{22}$$

The proof shows that the neural network \mathcal{Q} with kernels $(\Psi, \tilde{\Psi})$ is well trained to represent individual artifact $g^{(i)}$, which is the cupping artifact with a dominant low-frequency Fourier support $\mathcal{F}_{\text{low}}(c_j^{(i)})$ (see Fig. 4(a)) or the image noise with a dominant high-frequency Fourier support $\mathcal{F}_{\text{high}}(n^{(i)})$ (see Fig. 4(b)), satisfying $\text{RANK}\mathbb{H}_d(\bar{g}^{(i)}) \leq r_{\text{max}}$ where $\bar{g}^{(i)}$ is any feasible noise.

Here, we consider that the neural network \mathcal{Q} is fixed and recovers the coupled artifact $k^{(i)} = c_j^{(i)} + n^{(i)}$ instead of the individual artifact $g^{(i)}$, and the cupping artifact $c_j^{(i)}$ and the image noise $n^{(i)}$ with opposite Fourier supports are coupled together as shown in Fig. 1(b). Then, the kernels $(\Psi, \tilde{\Psi})$ do not satisfy with Eq. 10(b) since $\text{RANK}\mathbb{H}_d(\bar{k})$ is greater than the upper bound of the rank r_{max} , i.e.

$$\begin{aligned} \text{RANK}\mathbb{H}_d(\bar{n}) \leq r_{\text{max}} < \text{RANK}\mathbb{H}_d(\bar{k}) \leq r_{\text{max}}^* \simeq d, \\ (\text{resp. } \text{RANK}\mathbb{H}_d(\bar{c}_j) \leq r_{\text{max}} < \text{RANK}\mathbb{H}_d(\bar{k}) \leq r_{\text{max}}^* \simeq d) \end{aligned} \tag{23}$$

where \bar{k} is any feasible coupled noise and r_{max}^* denotes the upper bound of the rank of Hankel structured matrix constructed by the coupled noise \bar{k} . Since the Fourier support of the coupled noise $k^{(i)} \in \mathbb{R}^n$ fills most of the Fourier domain, its rank of the Hankel structured matrix is close to the length of the signal based on Eq. 9. To match the low-rank condition, the convolutional filter length d must exceed the length of the signal, but it is not efficient to build a network architecture that satisfies the filter length d equal to the signal length. Therefore, the neural network \mathcal{Q} no longer satisfies the deep convolutional framelets and fails to reconstruct a clean image $\bar{f}_j = q_j - \bar{k}$ from a multi-noisy image $q_j = f_j + k$.

4.2. End-to-end deep learning using dual-domain CNN

Then, is there an algorithm that satisfies deep convolutional framelets even though the image $q^{(i)}$ is contaminated by artifacts with both opposite properties? An easy way to get a solution to the question is to separate $T(n_j^{(i)}) \in \mathcal{S}_n$ and $T(c_j^{(i)}) \in \mathcal{S}_c$ using any transform function T for the coupled artifacts $n_j^{(i)} + c_j^{(i)}$ in image domain, where \mathcal{S}_n and \mathcal{S}_c are domains transformed from the image noise $n^{(i)}$ and the cupping artifact $c^{(i)}$ using the transform function T , respectively, and are domains that do not overlap each other. In projection domain, the above condition is exactly achieved, the image

Table 1. Objective functions in terms of various network architectures.

	\odot	Hadamard product	\mathcal{R}^{-1}	inverse Radon transform
(a) <i>Symbols</i>	\mathcal{J}	ROI mask in image domain	\mathcal{T}	truncation mask in projection domain
	f	noise-free image	q	FBP image
	p	collapsed projection	h	projection noise
	n	image noise	c	cupping artifact
	Ψ	encoder in backbone network	$\tilde{\Psi}$	decoder in backbone network
	$\tilde{\Psi}_*$	bridge modules $*$ \in [noise, extra] connected to decoder	\mathcal{Q}_{img}	image-domain CNN
	\mathcal{Q}_{prj}^*	projection-domain CNN with bridge module $*$ \in [noise, extra]		
(b) $\mathcal{L}_{\text{U-Net}}^{img}$	$\min_{(\Psi, \tilde{\Psi}, \tilde{\Psi}_{img})}$	$\sum_{i=1}^N \left\ \mathcal{J}^{(i)} \odot (q^{(i)} - f^{(i)}) - \mathcal{J}^{(i)} \odot \mathcal{Q}_{img} \left(q^{(i)}; \Psi, [\tilde{\Psi}, \tilde{\Psi}_{img}] \right) \right\ ^2$		
(c) $\mathcal{L}_{\text{U-Net}}^{prj}$	$\min_{(\Psi, \tilde{\Psi}, \tilde{\Psi}_{noise})}$	$\sum_{i=1}^N \left\ \mathcal{J}^{(i)} \odot (p^{(i)} - y^{(i)}) - \mathcal{T}^{(i)} \odot \mathcal{Q}_{prj}^{noise} \left(p^{(i)}; \Psi, [\tilde{\Psi}, \tilde{\Psi}_{noise}] \right) \right\ ^2$		
	$+$	$\min_{(\Psi, \tilde{\Psi}, \tilde{\Psi}_{extra})} \sum_{i=1}^N \left\ \mathcal{J}^{(i)} \odot f^{(i)} - \mathcal{J}^{(i)} \odot \mathcal{R}^{-1} \left(\mathcal{T}^{(i)} \odot (p^i - \bar{h}^{(i)}) + (1 - \mathcal{T}^{(i)}) \odot \mathcal{Q}_{prj}^{extra} \left(p^{(i)}; \Psi, [\tilde{\Psi}, \tilde{\Psi}_{extra}] \right) \right) \right\ ^2$		
(d) $\mathcal{L}_{\text{W-Net}}$	$\min_{(\Psi^1, \tilde{\Psi}^1, \tilde{\Psi}_{img}^1)}$	$\sum_{i=1}^N \left\ \mathcal{J}^{(i)} \odot (q^{(i)} - f^{(i)}) - \mathcal{J}^{(i)} \odot \mathcal{Q}_{img^1} \left(q^{(i)}; \Psi^1, [\tilde{\Psi}^1, \tilde{\Psi}_{img}^1] \right) \right\ ^2$		
	$+$	$\min_{(\Psi^2, \tilde{\Psi}^2, \tilde{\Psi}_{img}^2)}$	$\sum_{i=1}^N \left\ \mathcal{J}^{(i)} \odot (\bar{q}^{(i)} - f^{(i)}) - \mathcal{J}^{(i)} \odot \mathcal{Q}_{img^2} \left(\bar{q}^{(i)}; \Psi^2, [\tilde{\Psi}^2, \tilde{\Psi}_{img}^2] \right) \right\ ^2$,	
		where \bar{q} denotes output of the first image-domain CNN $\mathcal{Q}_{img^1} \left(q^{(i)}; \Psi^1, [\tilde{\Psi}^1, \tilde{\Psi}_{img}^1] \right)$.		
(e) $\mathcal{L}_{\text{Dual-Net}}$	$\min_{(\Psi^1, \tilde{\Psi}^1, \tilde{\Psi}_{noise}^1)}$	$\sum_{i=1}^N \left\ \mathcal{J}^{(i)} \odot (p^{(i)} - y^{(i)}) - \mathcal{T}^{(i)} \odot \mathcal{Q}_{prj^1}^{noise} \left(p^{(i)}; \Psi^1, [\tilde{\Psi}^1, \tilde{\Psi}_{noise}^1] \right) \right\ ^2$		
	$+$	$\min_{(\Psi^1, \tilde{\Psi}^1, \tilde{\Psi}_{extra}^1)}$	$\sum_{i=1}^N \left\ \mathcal{J}^{(i)} \odot f^{(i)} - \mathcal{J}^{(i)} \odot \mathcal{R}^{-1} \left(\mathcal{T}^{(i)} \odot (p^i - \bar{h}^{(i)}) + (1 - \mathcal{T}^{(i)}) \odot \mathcal{Q}_{prj^1}^{extra} \left(p^{(i)}; \Psi^1, [\tilde{\Psi}^1, \tilde{\Psi}_{extra}^1] \right) \right) \right\ ^2$	
	$+$	$\min_{(\Psi^2, \tilde{\Psi}^2, \tilde{\Psi}_{img}^2)}$	$\sum_{i=1}^N \left\ \mathcal{J}^{(i)} \odot (\bar{q}^{(i)} - f^{(i)}) - \mathcal{J}^{(i)} \odot \mathcal{Q}_{img^2} \left(\bar{q}^{(i)}; \Psi^2, [\tilde{\Psi}^2, \tilde{\Psi}_{img}^2] \right) \right\ ^2$,	
		where $\bar{h} = \mathcal{Q}_{prj^1}^{noise} \left(p^{(i)}; \Psi^1, [\tilde{\Psi}^1, \tilde{\Psi}_{noise}^1] \right)$ denotes estimated projection noise from $\mathcal{Q}_{prj^1}^{noise}$ and		
		$\bar{q} = \mathcal{R}^{-1} \left(\mathcal{T}^{(i)} \odot (p^i - \bar{h}^{(i)}) + (1 - \mathcal{T}^{(i)}) \odot \mathcal{Q}_{prj^1}^{extra} \left(p^{(i)}; \Psi^1, [\tilde{\Psi}^1, \tilde{\Psi}_{extra}^1] \right) \right)$ denotes estimated FBP image from $\mathcal{Q}_{prj^1}^{extra}$.		

noise $n_j^{(i)}$ is transformed to the projection noise $h_{\mathcal{T}}$ inside a truncation mask \mathcal{T} , and the cupping artifact $c_j^{(i)}$ is described as a null space outside the truncation mask $(1 - \mathcal{T})$. In other words, the low-dose CT problem is modified from removing the image noise $n^{(i)}$ in image domain (see LHS of Eq. 24) to eliminating the projection noise $h^{(i)}$ in projection domain (see RHS of Eq. 24) and can be represented by

$$\arg \min_{\bar{n}_{\mathcal{J}} \in \mathcal{N}_r} \left\| n_{\mathcal{J}} - \bar{n}_{\mathcal{J}} \right\|_{\mathcal{J}=\mathbf{1}}^2 \rightsquigarrow \arg \min_{\bar{h}_{\mathcal{J}} \in \mathcal{H}_r} \left\| h_{\mathcal{J}} - \bar{h}_{\mathcal{J}} \right\|_{\mathcal{J}=\mathbf{1}}^2. \quad (24)$$

The interior tomography can be also represented from eliminating the cupping artifact $c_j^{(i)}$ of image domain (see LHS of Eq. 25) to estimating the feasible function \bar{z} of projection domain outside truncated region $(1 - \mathcal{T})$ (see RHS of Eq. 25), given by

$$\arg \min_{\bar{c}_{\mathcal{J}} \in \mathcal{C}_r} \left\| c_{\mathcal{J}} - \bar{c}_{\mathcal{J}} \right\|^2 \rightsquigarrow \arg \min_{\bar{z}_{(1-\mathcal{J})} \in \mathcal{Z}_r} \left\| f_{\mathcal{J}} - \mathcal{R}_{\mathcal{J}}^{-1} \left(y_{\mathcal{J}} + \bar{z}_{(1-\mathcal{J})} \right) \right\|^2. \quad (25)$$

In addition, its coupled problem can be represented by

$$\begin{aligned} & \arg \min_{\bar{g}_{\mathcal{T}} \in \mathcal{G}_r} \|(n_{\mathcal{T}} + c_{\mathcal{T}}) - \bar{g}_{\mathcal{T}}\|^2 \\ \rightsquigarrow & \arg \min_{\bar{h}_{\mathcal{T}} \in \mathcal{H}_r} \|h_{\mathcal{T}} - \bar{h}_{\mathcal{T}}\|^2 + \arg \min_{\bar{z}_{(1-\mathcal{T})} \in \mathcal{Z}_r} \|f_{\mathcal{T}} - \mathcal{R}_{\mathcal{T}}^{-1}(y_{\mathcal{T}} + \bar{z}_{(1-\mathcal{T})})\|^2. \end{aligned} \quad (26)$$

Most importantly, while both the cupping artifact $c_{\mathcal{T}}$ and the image noise $n_{\mathcal{T}}$ exist inside ROI in image domain, each artifact is separated inside and outside the measured region \mathcal{T} in projection domain. Because of this, the capacity of the neural network \mathcal{Q} is fixed, but it is possible to apply low-rank constraints to individual regions while satisfying the theory of the deep convolutional framelets.

To enforce the condition represented by the right-hand side of Eq. 26, we propose a projection-domain CNN \mathcal{Q}_{prj} in Fig. 2(b) and its objective function is defined in Table. 1(c). The objective function consists of two terms, and the first term leads to an estimation of projection noise using $\mathcal{Q}_{prj}^{noise}$ inside the projection data but the second term induces extrapolation using $\mathcal{Q}_{prj}^{extra}$ outside the projection data to eliminate the cupping artifacts in image domain. In addition, an unrolled network scheme is applied after a single network such as the image-domain CNN \mathcal{Q}_{img} and the projection-domain CNN \mathcal{Q}_{prj} in order to improve performance and its stability [35]. In the paper, we used an image-domain CNN \mathcal{Q}_{img^2} as a second network in an unrolled scheme because a count-domain CNN paper [36] has shown that the CNN unfolded in the measurement domain is not superior to the CNN unfolded in both the image domain and the count domain. Specifically, the proposed network in Fig. 2(d) is unrolled in different domains, and the first is the projection domain and the second is the image domain. Details of the objective function of the proposed network are described in Table. 1(e). Similar to the proposed network, a W-Net in Fig. 2(c) is the two-times unrolled version of the image-domain CNN \mathcal{Q}_{img} , and its objective function is formulated in Table. 1(d).

5. Results

Fig. 6 shows the objective functions with respect to the trained networks such as U-Net, W-Net, and proposed network. Even though the U-Net has double-sized parameters than others, the objective curve sits on top of other curves. The W-Net and the proposed network have a similar number of parameters and their flowcharts except for the data domain applied to the first network, but the objective curve of the proposed network shows the lowest curve than the W-Net. Therefore, the projection-domain CNN is useful for solving a coupled low-dose ROI CT problem. Table. 2 shows the average NMSE and SSIM values of CNNs when applied to various low-dose ROI CTs. The proposed method produces the best NMSE and SSIM values than other methods. Next, the W-Net followed the performance of the proposed method, and U-Net had the lowest improvement over the others. However, when a label with an infinite number of incident photons and truncated ratio of 0% is used as an input, the W-Net has been showed to perform worse than U-Net due to overestimation as shown in Table. 2. Interestingly, the U-Net has twice the parameters of the others but has the lowest improvement. The

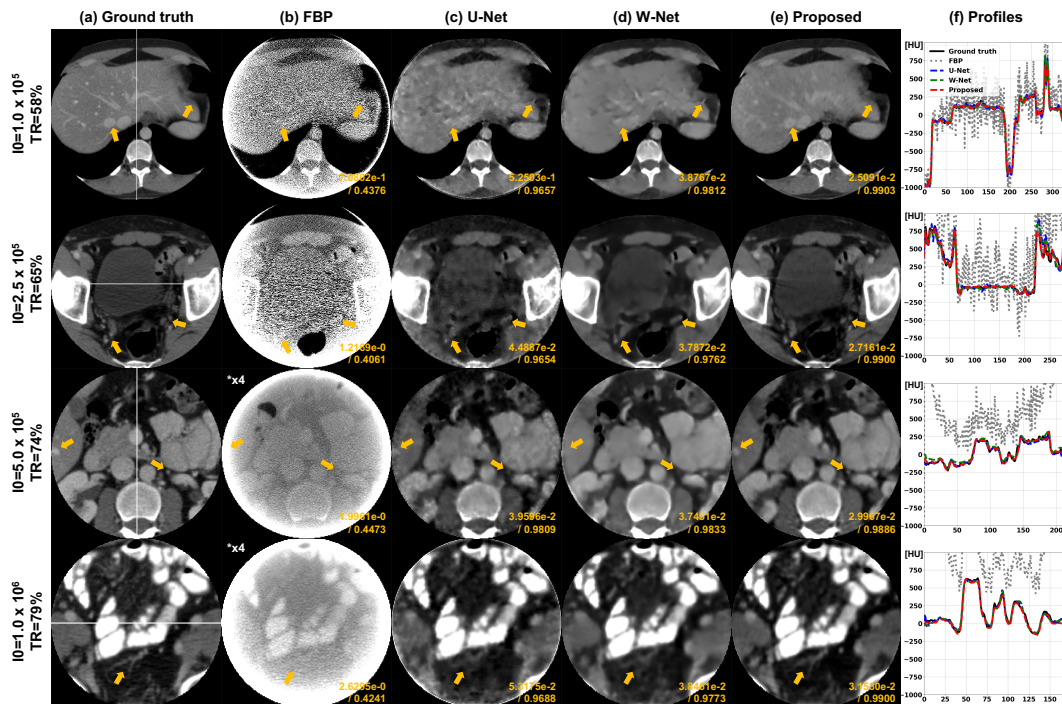


Figure 7. (a) Ground truth and reconstructed images by (b) FBP, (c) U-Net, (d) W-Net, and (e) proposed method. (f) Profiles along the white line on the results. From top to bottom, the number of photons gradually decreases, but the truncated ratio increases. The intensity range was set to $(-150, 400)$ [HU]. *x4 denotes that a window scale is magnified four times. NMSE / SSIM values are written at the corner.

trade-offs between the number of parameters and unrolled network architecture will be discussed later in Section 6.4.

Fig. 7 shows the reconstructed results by FBP, U-Net, W-Net, and proposed network in terms of various low-dose ROI CTs. When the number of photons and the size of ROIs are too small, the U-Net does not remove the artifacts clearly, so the reconstructed images from U-Net remain distorted artifacts. Although the W-Net produces better results than the U-Net, the reconstructed images are so blurry in many areas that small structures and textures are not preserved. In contrast to the U-Net and the W-Net, which are image-domain CNNs, the proposed method preserves not only the small structures but also the textures of the images and shows the lowest NMSE values than the other methods. Despite both the W-Net and the proposed network use the two-times unrolled networks, the proposed network shows significant improvement over the W-Net. The important reason to improve the performance of the proposed network is that the proposed network uses a projection-domain CNN as the first network and satisfies the theory of deep convolutional framelets, whereas the W-Net does not meet the theory.

Table 2. Quantitative comparison with respect to various ROIs and # of photons.

The number of incident photons		NMSE ($\times 10^{-2}$)	Ratios of truncated detectors					
			0%	44%	58%	65%	74%	79%
The number of incident photons	∞	FBP	-	24.025	74.370	117.79	193.58	270.48
		U-Net	0.9774	1.6771	2.1493	3.0715	4.1914	7.8876
		W-Net	1.0173	1.5146	1.7644	2.0412	2.4303	3.7594
		Proposed	0.7106	0.9121	1.1092	1.2532	2.0675	2.9322
	1.0×10^7	FBP	3.5022	24.260	74.430	117.83	193.61	270.50
		U-Net	1.5299	1.8806	2.3331	3.2274	4.2828	7.9061
		W-Net	1.5006	1.6979	1.9421	2.1864	2.5682	3.8554
		Proposed	1.0395	1.1016	1.2581	1.3891	2.1690	3.0162
	1.0×10^6	FBP	1.1332	26.379	75.026	118.23	193.89	270.72
		U-Net	2.4703	2.5721	2.9801	3.7945	4.6882	8.1475
		W-Net	2.2903	2.2889	2.4881	2.6984	3.0405	4.2085
		Proposed	1.5485	1.5067	1.6520	1.7864	2.4887	3.2861
	5.0×10^5	FBP	15.950	28.457	75.680	118.68	194.20	270.97
		U-Net	2.8875	2.9551	3.3360	4.1162	4.9620	8.2956
		W-Net	2.6322	2.6075	2.7797	2.9884	3.3216	4.4191
		Proposed	1.7481	1.6886	1.8467	1.9885	2.6662	3.4337
2.5×10^5	FBP	22.427	32.085	76.961	119.56	194.81	271.47	
	U-Net	3.4469	3.4788	3.8156	4.5546	5.4141	8.6357	
	W-Net	3.0635	3.0336	3.1664	3.3856	3.6960	4.7537	
	Proposed	1.9800	1.9049	2.0818	2.2311	2.8875	3.6211	
1.0×10^5	FBP	34.959	40.694	80.618	122.15	196.66	272.94	
	U-Net	4.6303	4.5646	4.7933	5.5142	6.5089	9.6548	
	W-Net	3.8775	3.8302	3.9137	4.1427	4.4446	5.5535	
	Proposed	2.3678	2.2633	2.4671	2.6180	3.2606	3.9583	
The number of incident photons		SSIM	Ratios of truncated detectors					
			0%	44%	58%	65%	74%	79%
The number of incident photons	∞	FBP	1.0000	0.9296	0.8383	0.7912	0.6844	0.5583
		U-Net	0.9979	0.9937	0.9930	0.9904	0.9885	0.9703
		W-Net	0.9976	0.9950	0.9951	0.9943	0.9925	0.9876
		Proposed	0.9990	0.9979	0.9982	0.9978	0.9962	0.9933
	1.0×10^7	FBP	0.9726	0.9058	0.8119	0.7637	0.6488	0.5229
		U-Net	0.9952	0.9922	0.9911	0.9880	0.9851	0.9663
		W-Net	0.9952	0.9939	0.9935	0.9927	0.9897	0.9847
		Proposed	0.9978	0.9970	0.9971	0.9966	0.9943	0.9907
	1.0×10^6	FBP	0.7952	0.7578	0.6560	0.6068	0.4915	0.3795
		U-Net	0.9895	0.9874	0.9845	0.9800	0.9746	0.9517
		W-Net	0.9906	0.9901	0.9886	0.9874	0.9821	0.9752
		Proposed	0.9953	0.9947	0.9941	0.9932	0.9893	0.9840
	5.0×10^5	FBP	0.6833	0.6702	0.5688	0.5223	0.4191	0.3200
		U-Net	0.9868	0.9845	0.9809	0.9756	0.9685	0.9435
		W-Net	0.9886	0.9880	0.9860	0.9845	0.9782	0.9703
		Proposed	0.9942	0.9937	0.9925	0.9914	0.9868	0.9807
2.5×10^5	FBP	0.5508	0.5714	0.4750	0.4339	0.3477	0.2649	
	U-Net	0.9828	0.9803	0.9757	0.9694	0.9599	0.9316	
	W-Net	0.9859	0.9849	0.9826	0.9805	0.9732	0.9637	
	Proposed	0.9929	0.9925	0.9906	0.9891	0.9838	0.9767	
1.0×10^5	FBP	0.3707	0.4442	0.3631	0.3315	0.2684	0.2075	
	U-Net	0.9719	0.9698	0.9629	0.9548	0.9401	0.9045	
	W-Net	0.9798	0.9787	0.9763	0.9733	0.9638	0.9521	
	Proposed	0.9905	0.9903	0.9872	0.9852	0.9787	0.9699	

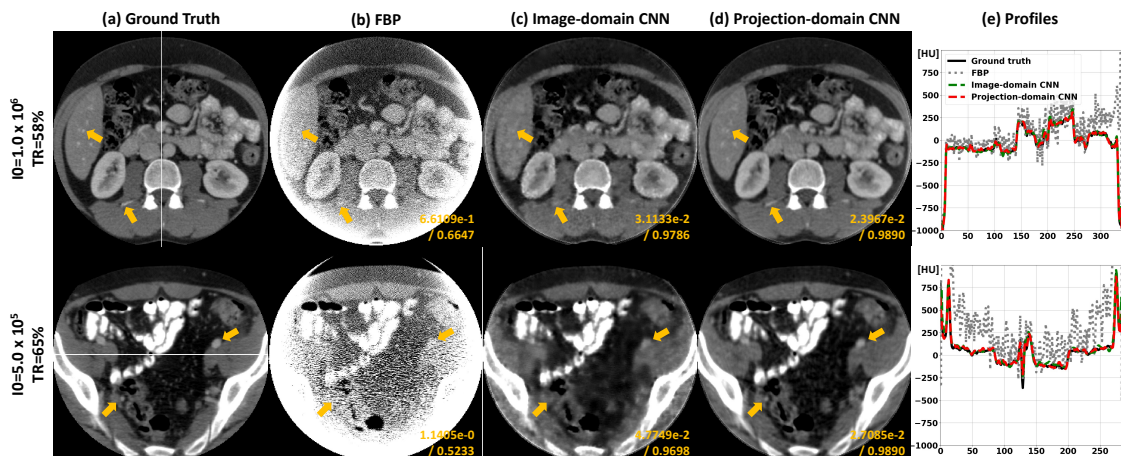


Figure 8. (a) Ground truth and reconstructed images by (b) FBP, (c) image-domain CNN and (d) projection-domain CNN. (e) Profiles along the white lines on the results. First and second rows show reconstructed images from $I_0 = 1.0 \times 10^6$ with 58% truncated detectors and $I_0 = 5.0 \times 10^5$ with 65% truncated detectors, respectively. The intensity range was set to $(-150, 400)$ [HU]. NMSE / SSIM values are written at the corner.

6. Discussion

6.1. Network efficiency according to training domain

In Sec. 5, we showed that the proposed network outperforms the image-domain networks like U-Net and W-Net. The reason for its excellent performance is that the proposed method approaches it as a way to find decoupled solutions in projection domain even though the solution is coupled in image domain. To verify our claim, quantitative metrics are calculated for a single image-domain CNN \mathcal{Q}_{img} (see Fig. 2(a)) used as the first network of the trained W-Net and a single projection-domain CNN \mathcal{Q}_{prj} (see Fig. 2(b)) used as the first network of the trained proposed network, and the average NMSE and SSIM values are described in Table 3. The projection-domain CNN \mathcal{Q}_{prj} outperforms the image-domain CNN \mathcal{Q}_{img} , and Fig. 8 shows reconstructed images for each network. Even though the reconstructed images from the image-domain CNN \mathcal{Q}_{img} are not texture-preserved and suffer from severe blurring in many areas, the projection-domain CNN \mathcal{Q}_{prj} removes the artifacts such as the image noise and the cupping artifact and preserves the underlying structure. For this result, because the image size is 512×512 but the projection data is 720×1440 , we can doubt about an unfairness in the size of the training dataset between image domain and projection domain. However, the projection data can be transformed to the image data using a linear function such as the filtered backprojection (FBP) operation. From an information perspective, this means that the information of the projection data is similar to the information of the image data. Therefore, although many researchers use the image-domain CNN \mathcal{Q}_{img} to solve CT problems, we argue that the projection-domain CNN \mathcal{Q}_{prj} , consisting of two bridge modules that estimate the projection noise inside measured region \mathcal{T} and extrapolation

Table 3. Quantitative comparison between image- and projection-domain CNNs.

		NMSE ($\times 10^{-2}$)	Ratios of truncated detectors					
			0%	44%	58%	65%	74%	79%
The number of incident photons	∞	I-domain	1.0780	1.8387	2.7758	3.5036	4.3792	7.9992
		P-domain	0.5346	1.1330	1.7984	2.3472	4.0934	6.5316
	1.0×10^7	I-domain	1.5831	2.0245	2.9153	3.6079	4.4841	8.0629
		P-domain	1.0127	1.3645	1.9474	2.4774	4.1746	6.5956
	1.0×10^6	I-domain	2.5743	2.7199	3.4837	4.0808	4.9567	8.3683
		P-domain	1.6421	1.8032	2.2945	2.8109	4.4102	6.7657
	5.0×10^5	I-domain	3.0332	3.1350	3.7999	4.3631	5.2635	8.6015
		P-domain	1.8966	2.0086	2.4715	2.9798	4.5435	6.8480
	2.5×10^5	I-domain	3.6433	3.7098	4.2361	4.7376	5.6669	8.9502
		P-domain	2.2099	2.2664	2.6960	3.1917	4.7167	6.9653
	1.0×10^5	I-domain	4.9174	4.8833	5.1807	5.5345	6.4666	9.9097
		P-domain	2.7906	2.7455	3.1177	3.5908	5.0470	7.2115
			SSIM	Ratios of truncated detectors				
				0%	44%	58%	65%	74%
The number of incident photons	∞	I-domain	0.9973	0.9930	0.9895	0.9863	0.9856	0.9697
		P-domain	0.9994	0.9967	0.9961	0.9941	0.9889	0.9784
	1.0×10^7	I-domain	0.9946	0.9916	0.9877	0.9845	0.9822	0.9659
		P-domain	0.9978	0.9953	0.9945	0.9924	0.9863	0.9748
	1.0×10^6	I-domain	0.9884	0.9866	0.9806	0.9774	0.9713	0.9510
		P-domain	0.9947	0.9925	0.9908	0.9881	0.9801	0.9665
	5.0×10^5	I-domain	0.9853	0.9833	0.9768	0.9734	0.9651	0.9424
		P-domain	0.9932	0.9911	0.9889	0.9859	0.9767	0.9621
	2.5×10^5	I-domain	0.9805	0.9782	0.9714	0.9677	0.9566	0.9306
		P-domain	0.9912	0.9892	0.9863	0.9829	0.9722	0.9561
	1.0×10^5	I-domain	0.9671	0.9654	0.9581	0.9546	0.9379	0.9045
		P-domain	0.9863	0.9850	0.9807	0.9763	0.9623	0.9423

* I-domain and P-domain are defined as the first network for the W-Net and the proposed.

map outside measured region $(1 - \mathcal{J})$, is more useful than the image-domain CNN Q_{img} because the projection domain provides a more efficient low-rank property than the image domain. In addition, the numerical results support our claim as shown in Table. 3 and Fig. 8.

6.2. Low rankness according to training domain

In the section 6.1, we confirmed that a projection-domain CNN shows better performance than an image-domain CNN. Here, to verify our claim that the projection-domain CNN can satisfy better low rank properties of the Hankel structured matrix than the image-domain CNN, we computed singular values of the Hankel structured matrix of the last feature maps of each backbone network, and the results were plotted in Fig. 9. As with the previous section 6.1, the projection-domain CNN performs better than the image-domain CNN in similar network architectures because the computed singular value spectra in the projected-domain CNN is lower than the image-domain CNN. Therefore, based on the Figs. 8 and 9 and Table. 3, we verified that the projection-

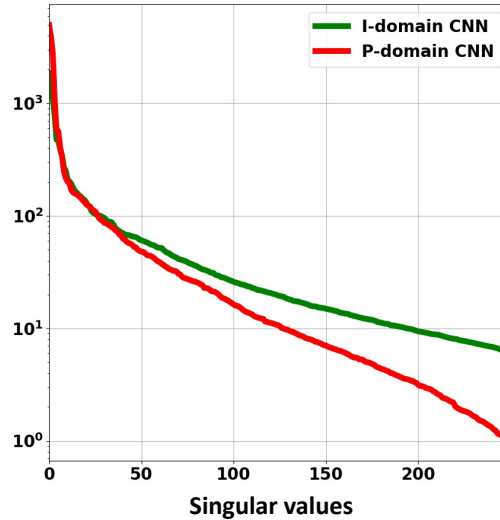


Figure 9. Singular value spectra of the Hankel structured matrix of the last feature maps of the backbone network according to the image-domain CNN (green) and the projection-domain CNN (red).

domain CNN is suitable for the low rankness and offers better performance than the image-domain CNN.

6.3. Interior tomography vs. low-dose CT

The proposed method was developed to solve a CT problem combining interior tomography and low-dose CT and showed superior performance than others as shown in Table. 2 and Fig. 7. Here, we can be wondering that how the performance differs when the problem is already isolated. Tables. 4 and 5 show PSNR values with respect to interior tomography without projection noise ($I0 = \infty$) and low-dose CT without a detector truncation, respectively. Interestingly, the CT problem has already been decoupled into interior tomography and low-dose CT, but the proposed method is still superior to the other methods. Fig. 10 shows the reconstructed images from decoupled CT systems.

For the interior tomography in Fig. 10(i), the proposed network preserved details and textures of the images regardless of the truncated size. However, the U-Net and the W-Net showed high-quality reconstructed images when a ROI is large, but slightly blurry when the ROI is small. Extrapolation method, which is an existing method, was also performed to solve the interior tomography problem (see Fig. 10(i)(c)). For large ROI, the extrapolation method moderately mitigated cupping artifacts, but for small ROI, it did not work. MBIR method with TV penalty showed more stable results than the extrapolation method, but did not exceed the DL performance. When the low-dose CT in Fig. 10(ii), the U-Net and the W-Net removed image noise as well as small

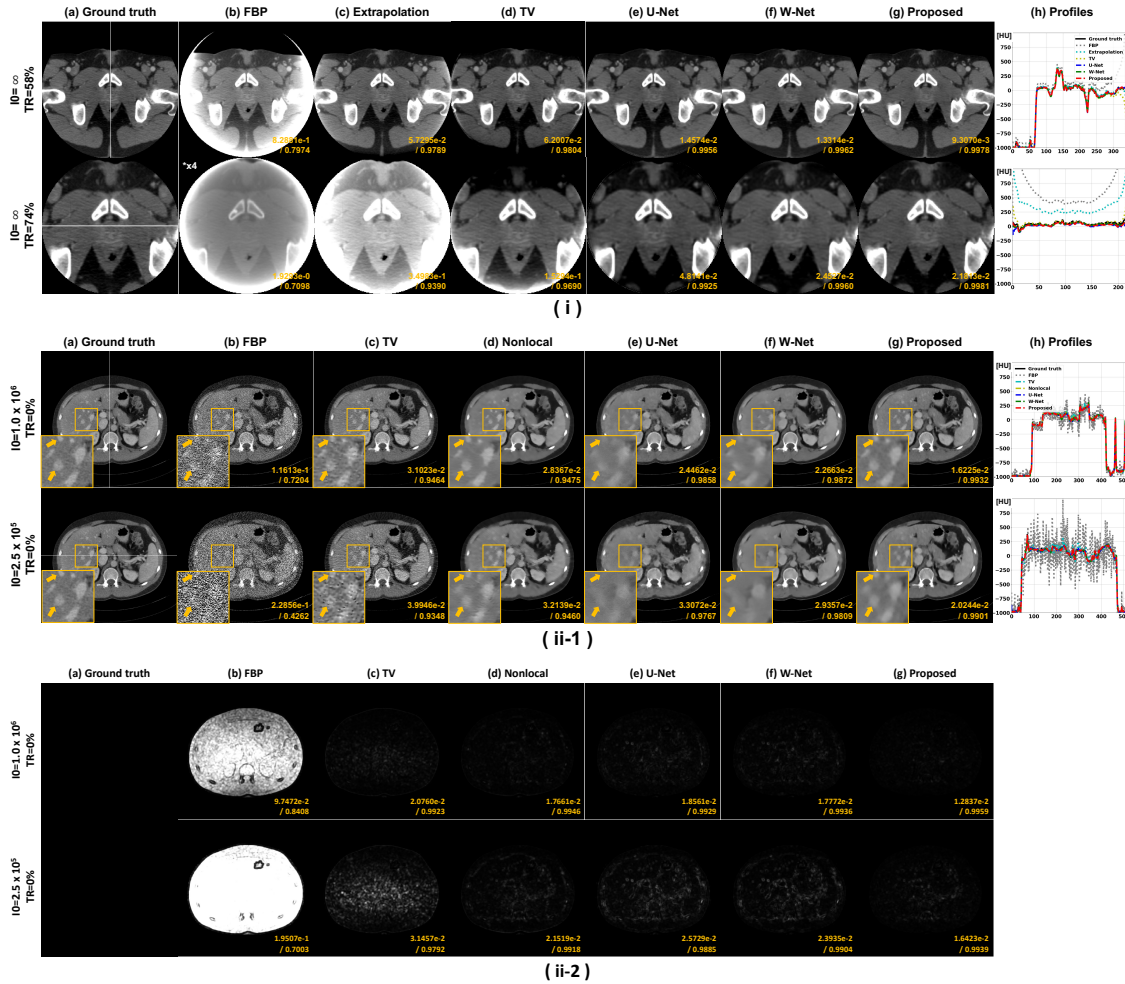


Figure 10. Reconstructed images from (i) interior tomography with (58%, 74%) truncated ratios and (ii-1) low-dose CT with $I_0 = (1.0 \times 10^6, 2.5 \times 10^5)$. (ii-2) SSIM maps calculated from in-body regions of (ii-1). The intensity range was set to $(-150, 400)$ [HU]. *x4 denotes that a window scale is magnified four times. NMSE / SSIM values are written at the corner.

tissues, but the proposed method preserved the small tissues well, and only removed image noise. Specifically, MBIR method with TV penalty was performed to remove the image noise. Compared to the U-Net and the W-Net, the TV method preserves details better despite noise remaining in the reconstructed image as shown in Fig. 10(ii)(c). Nonlocal prior method[37], which is the AAPM challenge winning algorithm, preserved details better than U-Net and W-Net and removed the image noises better than TV method. However, the NMSE and SSIM value do not seem to reflect the well-corrected image quality of the nonlocal prior method. To clarify the image quality evaluation when the low-dose measurement, the NMSE and SSIM values were re-calculated within body regions. Fig. 10(ii-2) shows the SSIM map inside body regions, and the high-intensity represents the proportion of miss-matched structure with ground truth. Although the nonlocal prior method outperformed the TV, U-Net, and W-Net methods, the proposed

Table 4. Quantitative comparison with respect to interior tomography.

PSNR [dB]		Ratios of truncated detectors					
		0%	44%	58%	65%	74%	79%
Incident photons	Extra.	-	36.1378	34.4970	27.3378	15.5640	8.7176
	TV	-	38.4084	29.3277	29.0841	24.4248	18.7840
	U-Net	50.5815	45.1681	42.0854	38.9915	35.0328	28.8829
	W-Net	50.2332	46.0520	43.6709	41.9147	39.2676	34.5895
	Proposed	53.3537	50.4824	47.6772	46.3142	41.0630	37.2672

Table 5. Quantitative comparison with respect to low-dose CT.

PSNR [dB]		The number of incident photons					
		∞	1.0×10^7	1.0×10^6	5.0×10^5	2.5×10^5	1.0×10^5
Truncated rate	TV	-	41.6881	39.9633	39.4789	37.4864	33.2091
	Nonlocal	-	42.6110	41.3111	40.5736	39.5787	37.8072
	0% U-Net	50.5818	46.6985	42.5485	41.2001	39.6735	37.1377
	W-Net	50.2332	46.8628	43.1995	41.9968	40.6882	38.6591
	Proposed	53.3537	50.0518	46.5811	45.5246	44.4409	42.8878

method achieved best performance than the nonlocal prior method.

6.4. Unrolled neural network architecture

The single CNNs in Figs. 2(a, b) are recognized as one-time unrolled CNNs, even though their training domains are different. From the previous point of view, the W-Net in Fig. 2(c) and the proposed network in Fig. 2(d) are the two-times unrolled CNNs. However, the W-Net is stretched only in the image domain, but the proposed network is unfolded sequentially in the projection domain and the image domain. Comparing Table. 2 and Table. 3, the two-times unrolled CNNs outperforms the one-time unrolled CNNs. Since the two-times unrolled CNNs have twice the parameter size than the one-times unrolled CNNs, it can be taken for granted. However, the U-Net has two-times the parameters of the W-Net, but the W-Net shows better performance than the U-Net. In a comparative study of U-Net and W-Net, we found that a sequence of several DLs with low expressibility shows better performance than a single DL with high expressibility. In addition, both the W-Net and the proposed network are the two-times unrolled CNN, but as confirmed in Section 6.1, the proposed method initially unfolded in projection domain is more efficient than the W-Net.

7. Conclusion

In this paper, we proposed the novel and efficient low-dose interior CT reconstruction. Due to the coupled artifacts, we have shown that image-domain CNNs do not satisfy the low rankness, which can degrade the performance. Thus, instead of using the image-domain CNN, we decoupled inside and outside measured regions in the projection

domain to efficiently estimate separated solutions. To address the decoupling, we proposed the novel end-to-end deep learning method consisting of projection- and image-domain CNNs referred to as the dual-domain CNNs. Specifically, the projection-domain CNN solves two major problems; (1) noise from inside the measured region and (2) extrapolation from outside the measured region. Then, the image-domain CNN further improved the image quality. Our results demonstrated that the proposed method outperformed the model-based reconstruction methods and the conventional image-domain CNNs.

References

- [1] Nikhil Bharat Shah and Shari L Platt. Alara: is there a cause for alarm? reducing radiation risks from computed tomography scanning in children. *Current opinion in pediatrics*, 20(3):243–247, 2008.
- [2] Johan Nuyts, Bruno De Man, Jeffrey A Fessler, Wojciech Zbijewski, and Freek J Beekman. Modelling the physics in the iterative reconstruction for transmission computed tomography. *Physics in Medicine & Biology*, 58(12):R63, 2013.
- [3] Jiang Hsieh, Ed Chao, J Thibault, Brian Grekowicz, Amy Horst, Scott McOlash, and TJ Myers. Algorithm to extend reconstruction field-of-view. In *2004 2nd IEEE International Symposium on Biomedical Imaging: Nano to Macro (IEEE Cat No. 04EX821)*, pages 1404–1407. IEEE, 2004.
- [4] J Hsieh, E Chao, J Thibault, B Grekowicz, A Horst, S McOlash, and TJ Myers. A novel reconstruction algorithm to extend the ct scan field-of-view. *Medical physics*, 31(9):2385–2391, 2004.
- [5] Hengyong Yu and Ge Wang. Compressed sensing based interior tomography. *Physics in medicine & biology*, 54(9):2791, 2009.
- [6] John Paul Ward, Minji Lee, Jong Chul Ye, and Michael Unser. Interior tomography using 1d generalized total variation. part i: Mathematical foundation. *SIAM Journal on Imaging Sciences*, 8(1):226–247, 2015.
- [7] Minji Lee, Yoseob Han, John Paul Ward, Michael Unser, and Jong Chul Ye. Interior tomography using 1d generalized total variation. part ii: Multiscale implementation. *SIAM Journal on Imaging Sciences*, 8(4):2452–2486, 2015.
- [8] Xiaochuan Pan, Emil Y Sidky, and Michael Vannier. Why do commercial ct scanners still employ traditional, filtered back-projection for image reconstruction? *Inverse problems*, 25(12):123009, 2009.
- [9] Junguo Bian, Jeffrey H Siewerdsen, Xiao Han, Emil Y Sidky, Jerry L Prince, Charles A Pelizzari, and Xiaochuan Pan. Evaluation of sparse-view reconstruction from flat-panel-detector cone-beam ct. *Physics in Medicine & Biology*, 55(22):6575, 2010.
- [10] Yang Lu, Jun Zhao, and Ge Wang. Few-view image reconstruction with dual dictionaries. *Physics in Medicine & Biology*, 57(1):173, 2011.
- [11] Kyungsang Kim, Jong Chul Ye, William Worstell, Jinsong Ouyang, Yothin Rakvongthai, Georges El Fakhri, and Quanzheng Li. Sparse-view spectral ct reconstruction using spectral patch-based low-rank penalty. *IEEE transactions on medical imaging*, 34(3):748–760, 2014.
- [12] Sajid Abbas, Taewon Lee, Sukyoung Shin, Rena Lee, and Seungryong Cho. Effects of sparse sampling schemes on image quality in low-dose ct. *Medical physics*, 40(11):111915, 2013.
- [13] Marcel Beister, Daniel Kolditz, and Willi A Kalender. Iterative reconstruction methods in x-ray ct. *Physica medica*, 28(2):94–108, 2012.
- [14] Sathish Ramani and Jeffrey A Fessler. A splitting-based iterative algorithm for accelerated statistical x-ray ct reconstruction. *IEEE transactions on medical imaging*, 31(3):677–688, 2011.

- [15] Kyong Hwan Jin, Michael T McCann, Emmanuel Froustey, and Michael Unser. Deep convolutional neural network for inverse problems in imaging. *IEEE Transactions on Image Processing*, 26(9):4509–4522, 2017.
- [16] Hyeon Lee, Jongha Lee, Hyeongseok Kim, Byungchul Cho, and Seungryong Cho. Deep-neural-network-based sinogram synthesis for sparse-view ct image reconstruction. *IEEE Transactions on Radiation and Plasma Medical Sciences*, 3(2):109–119, 2018.
- [17] Yoseob Han and Jong Chul Ye. Framing u-net via deep convolutional framelets: Application to sparse-view ct. *IEEE transactions on medical imaging*, 37(6):1418–1429, 2018.
- [18] Jelmer M Wolterink, Tim Leiner, Max A Viergever, and Ivana Išgum. Generative adversarial networks for noise reduction in low-dose ct. *IEEE transactions on medical imaging*, 36(12):2536–2545, 2017.
- [19] Hu Chen, Yi Zhang, Mannudeep K Kalra, Feng Lin, Yang Chen, Peixi Liao, Jiliu Zhou, and Ge Wang. Low-dose ct with a residual encoder-decoder convolutional neural network. *IEEE transactions on medical imaging*, 36(12):2524–2535, 2017.
- [20] Eunhee Kang, Junhong Min, and Jong Chul Ye. A deep convolutional neural network using directional wavelets for low-dose x-ray ct reconstruction. *Medical physics*, 44(10):e360–e375, 2017.
- [21] Yoseob Han, Jawook Gu, and Jong Chul Ye. Deep learning interior tomography for region-of-interest reconstruction. *arXiv preprint arXiv:1712.10248*, 2017.
- [22] Yoseob Han and Jong Chul Ye. One network to solve all rois: Deep learning ct for any roi using differentiated backprojection. *Medical Physics*, 46(12):e855–e872, 2019.
- [23] Jong Chul Ye, Yoseob Han, and Eunju Cha. Deep convolutional framelets: A general deep learning framework for inverse problems. *SIAM Journal on Imaging Sciences*, 11(2):991–1048, 2018.
- [24] Jiang Hsieh. *Computed tomography: principles, design, artifacts, and recent advances*, volume 114. SPIE press, 2003.
- [25] Yining Zhu, Mengliu Zhao, Yunsong Zhao, Hongwei Li, and Peng Zhang. Noise reduction with low dose ct data based on a modified rof model. *Optics express*, 20(16):17987–18004, 2012.
- [26] Jong Chul Ye and Woon Kyoung Sung. Understanding geometry of encoder-decoder cnns. In *International Conference on Machine Learning*, pages 7064–7073. PMLR, 2019.
- [27] Kyong Hwan Jin and Jong Chul Ye. Annihilating filter-based low-rank hankel matrix approach for image inpainting. *IEEE Transactions on Image Processing*, 24(11):3498–3511, 2015.
- [28] Kyong Hwan Jin and Jong Chul Ye. Sparse and low-rank decomposition of a hankel structured matrix for impulse noise removal. *IEEE Transactions on Image Processing*, 27(3):1448–1461, 2017.
- [29] Kyong Hwan Jin, Dongwook Lee, and Jong Chul Ye. A general framework for compressed sensing and parallel mri using annihilating filter based low-rank hankel matrix. *IEEE Transactions on Computational Imaging*, 2(4):480–495, 2016.
- [30] Dongwook Lee, Kyong Hwan Jin, Eung Yeop Kim, Sung-Hong Park, and Jong Chul Ye. Acceleration of mr parameter mapping using annihilating filter-based low rank hankel matrix (aloha). *Magnetic resonance in medicine*, 76(6):1848–1864, 2016.
- [31] Juyoung Lee, Kyong Hwan Jin, and Jong Chul Ye. Reference-free single-pass epi n yquist ghost correction using annihilating filter-based low rank h ankel matrix (aloha). *Magnetic resonance in medicine*, 76(6):1775–1789, 2016.
- [32] Olaf Ronneberger, Philipp Fischer, and Thomas Brox. U-net: Convolutional networks for biomedical image segmentation. In *International Conference on Medical image computing and computer-assisted intervention*, pages 234–241. Springer, 2015.
- [33] C McCollough. Tu-fg-207a-04: Overview of the low dose ct grand challenge. *Medical physics*, 43(6Part35):3759–3760, 2016.
- [34] Lifeng Yu, Maria Shiung, Dayna Jondal, and Cynthia H McCollough. Development and validation of a practical lower-dose-simulation tool for optimizing computed tomography scan protocols. *Journal of computer assisted tomography*, 36(4):477–487, 2012.

- [35] Fengyuan Jiao, Zhiguo Gui, Kunpeng Li, Hong Shangguang, Yanling Wang, Yi Liu, and Pengcheng Zhang. A dual-domain cnn-based network for ct reconstruction. *IEEE Access*, 9:71091–71103, 2021.
- [36] Taejoon Eo, Yohan Jun, Taeseong Kim, Jinseong Jang, Ho-Joon Lee, and Dosik Hwang. Kiki-net: cross-domain convolutional neural networks for reconstructing undersampled magnetic resonance images. *Magnetic resonance in medicine*, 80(5):2188–2201, 2018.
- [37] Kyungsang Kim, Georges El Fakhri, and Quanzheng Li. Low-dose ct reconstruction using spatially encoded nonlocal penalty. *Medical physics*, 44(10):e376–e390, 2017.